Lab on a Chip

PAPER

View Article Online
View Journal | View Issue

Cite this: *Lab Chip*, 2024, **24**, 5360

Observing root growth and signalling responses to stress gradients and pathogens using the bi-directional dual-flow RootChip†

Claudia Allan, [ac] Yiling Sun, [bc] Stephen C. Whisson, [d] Michael Porter, [d] Petra C. Boevink, [d] Volker Nock *[bc] and Claudia-Nicole Meisrimler *[a]

Plants respond to environmental stressors with adaptive changes in growth and development. Central to these responses is the role of calcium (Ca^{2+}) as a key secondary messenger. Here, the bi-directional dual-flow RootChip (bi-dfRC) microfluidic platform was used to study defence signalling and root growth. By introducing salinity as sodium chloride (NaCl) treatment *via* a multiplexed media delivery system (MMDS), dynamic gradients were created, mimicking natural environmental fluctuations. Signal analysis in *Arabidopsis thaliana* plants showed that the Ca^{2+} burst indicated by the G-CaMP3 was concentration dependent. A Ca^{2+} burst initiated in response to salinity increase, specifically within the stele tissue, for 30 seconds. The signal then intensified in epidermal cells directly in contact with the stressor, spreading directionally towards the root tip, over 5 minutes. Inhibition of propidium iodide (PI) stain transport through the xylem was observed following salinity increase, contrasting with flow observed under control conditions. The interaction of *Phytophthora capsici* zoospores with *A. thaliana* roots was also studied. An immediate directional Ca^{2+} signal was observed during early pathogen recognition, while a gradual, non-directional increase was observed in Orp1_roGFP fluorescent H_2O_2 levels, over 30 min. By adjusting the dimensions of the bi-dfRC, plants with varying root architectures were subjected to growth analysis. Growth reduction was observed in *A. thaliana* and *Nicotiana benthamiana* roots when exposed to salinity induced by 100 mM NaCl, while *Solanum lycopersicum* exhibited growth increase over 90 minutes at the same NaCl concentration. Furthermore, novel insights into force sensing in roots were gained through the engineering of displaceable pillars into the bi-dfRC channel. These findings highlight the vital role of controlling fluid flow in microfluidic channels in advancing our understanding of root physiology under stress conditions.

Received 8th August 2024,
Accepted 25th September 2024

DOI: 10.1039/d4lc00659c

rsc.li/loc

1 Introduction

Plant growth and development are influenced by a combination of environmental factors, including light, temperature, water availability, pathogens, and herbivores.[1] In response, plants undergo cellular, metabolic, and morphological changes while adjusting growth according to their surroundings.[2] This is often mediated by signalling molecules including hormones and secondary messengers.[3] These adaptive responses are, in part, regulated by a surge of cytosolic calcium ($[Ca^{2+}]_i$), exhibiting stress-specific spatiotemporal localisation in plant cells, tissues and organs.[4] Following influx of Ca^{2+}, EF-hand proteins such as calmodulin (CaM) and calmodulin-like proteins (CMLs) bind to Ca^{2+} and undergo a conformational change.[5] The Ca^{2+}-CaM complex subsequently interacts with target proteins, including protein kinases and other regulatory molecules, leading to responses reducing the impact of a given stressor.[6]

Upon high salinity or drought conditions, elevated Ca^{2+} levels activate Ca^{2+}-dependent protein kinases (CDPKs), which phosphorylate key components involved in abscisic acid (ABA) signalling, such as ion channels and transcription factors, leading to stomatal closure and water retention.[7] ABA and stomatal closure are also associated with pathogen responses, including *Pseudomonas*, which causes water soaking at the early stage of infections,[8] highlighting the link

[a] *School of Biological Sciences, University of Canterbury, Private Bag 4800, Christchurch, New Zealand. E-mail: claudia.meisrimler@canterbury.ac.nz; Tel: +64 33691019*
[b] *Department of Electrical and Computer Engineering, University of Canterbury, Private Bag 4800, Christchurch, New Zealand. E-mail: volker.nock@canterbury.ac.nz; Tel: + 64 33694303*
[c] *MacDiarmid Institute for Advanced Materials and Nanotechnology, PO Box 600, Wellington 6140, New Zealand*
[d] *Cell and Molecular Sciences, The James Hutton Institute, Invergowrie, Dundee DD2 5DA, Scotland, UK*

† Electronic supplementary information (ESI) available. See DOI: https://doi.org/10.1039/d4lc00659c

between drought, salt stress, and pathogen defense mechanisms. During pathogen attack, Ca^{2+} and nitric oxide (NO) act upstream of salicylic acid (SA) signalling, increasing the expression of pathogenesis-related (PR) genes,[9] and contributing to defence responses mediated by JA/ET pathways.[10] Ca^{2+}-dependent regulation of the cytoskeleton influences cell shape and growth.[11] Moreover, Ca^{2+} signals regulate the activity of microtubule-associated proteins (MAPs) and actin-binding proteins (ABPs), which regulate cytoskeletal organisation in response to external stress.[12]

Ca^{2+} signalling has previously been observed using genetically encoded fluorescent indicators.[13] Abiotic and biotic stress-induced Ca^{2+} bursts have been observed in both plant leaves and roots using various experimental arrangements.[14–18] The findings provided clues into stress-specific cellular Ca^{2+} signalling patterns and the precise tracking of systemic signals. Despite notable advances, details such as the root-specific spatiotemporal localisation of Ca^{2+} in response to a gradual stress accumulation as opposed to sudden treatment introduction, and its impact on the regulation of plant growth and development remains unclear.

Microfluidic technology has been successfully used as a tool to address plant biology, forming platforms to study stress-signals in various plant organs (shoots, leaves) of *Arabidopsis thaliana*,[19] and more recently in roots.[16,18] Microfluidic chip technology allows for precise control of treatment delivery within microchannels, including growth media containing macro- and micro-nutrients or stressors.[20] To date, multiple lab-on-a-chip (LoC) microfluidic devices for plant culture exist[21,22] including the plant on a chip,[23] RootArray,[24] PlantChip,[25] plant array chip,[26] millifluidic HOMEs networks,[27] dual-flow RootChip (dfRC),[16,28] petaloid root-growth microfluidic chip (PRGM),[29] stereolithography (SLA)-based next generation RootChip[30] and the rhizosphere-on-a-chip.[31]

In a previous study, we introduced the bi-directional dual-flow RootChip, a modification of the conventional dfRC.[32] This device was optimised for bi-directional osmotic stress treatments, enabling observation of directional Ca^{2+} signal responses in G-CaMP3-labeled *A. thaliana* plant lines. The fabrication process, flow matrix for media delivery, and chip dimensions were then described in detail, allowing successful root cultivation from various plant species in a microchannel up to 550 μm × 700 μm × 40 mm (W, H, L).[33] In this research, real-time switching of stress treatments within a microfluidic channel was achieved using the previously described and now further adapted flow matrix, renamed here as the multiplexed media delivery system (MMDS). This approach facilitated the study of adaptive mechanisms including root growth and signalling towards treatment switches, within a single sample. Here, we present distinct Ca^{2+} localisation patterns in *A. thaliana* roots towards linear gradients of NaCl. PI staining supports earlier findings about the limitations of water transport and growth reduction and provides insights into xylem movement in roots under salinity stress.[3] Multi-sized microfluidic chips highlighted differential growth responses towards NaCl treatment among different plant species, such as *A. thaliana*, *Nicotiana benthamiana*, and *Solanum lycopersicum*. This emphasises the bi-dfRCs potential use in crop plant studies. Additional modifications to the bi-dfRC include the integration of displaceable micropillars, enabling novel observation of the root tip growth force required for displacement and the signals triggered by touch. Finally, active injection of oomycete *Phytophthora capsici* zoospores induced Ca^{2+} signalling and H_2O_2 accumulation in the *A. thaliana* primary root, offering insights into the interactions between pathogens and plants. The findings presented in this research highlight the use of microfluidic technology to control fluids, enabling the study of plant stress adaptation and signalling mechanisms in response to environmental changes.

2 Methods

2.1 Fabrication of the bi-directional dual-flow RootChips with force sensing pillars

The bi-dfRC microfluidic devices were constructed according to the previously published detailed fabrication protocol.[18] The dimensions of the bi-dfRC design were modified to accommodate plants with varying root sizes following the standardised protocol (Files S1–S3†). All designs can be directly viewed in eDrawings Viewer (v31.3.0040) and modified in Solidworks (2023) or Fusion360 (v2.0.1649). To design the microfluidic chips, Mentor Graphics (v2020.1) was used. The new force-sensing version of the bi-dfRC was produced as described below. The force sensing bi-dfRC pillar array design contains 100 μm (h) and 30 μm (w) displaceable micropillars spanning the observation channel, shown in Fig. 1(a) and in the ESI† (Files S4 and S5).

Two-layer resist mold with raised channels and pillar cavities for replica molding were produced through photolithography. The first layer, which contains the channel outlines and triangle guiding pillar cavities, provides a 5 μm height spacer layer for the free-bending force sensing micropillars. The second layer has the same feature with the addition of sensing micropillar cavities. First, the bi-dfRC pattern was transferred to photo-masks (Nanofilm) using a laser mask writer (Heidelberg μPG101). A silicon wafer (single side 4″, Prime grade, WaferPro) was dehydrated, and oxygen plasma cleaned. A dry-film, negative-tone photoresist (ADEX 05, DJ Microlaminates) was applied using a laminator (Sky-335R6). The design of the first layer was then transferred into the photoresist layer through UV exposure (MA-6, SUSS MicroTec) at an exposure dose of 170 mJ cm^{-2} in vacuum contact mode with a filter (PL-360, Chroma). The spacer layer was achieved *via* a post-exposure-bake (PEB), development in propyleneglycol-monomethyletheracetate (PGMEA), rinsed with isopropyl alcohol (IPA) and dried by N_2. The second layer of the dry film photoresist (SUEX 100, DJ Microlaminates) was laminated onto the first spacer layer. After the post-lamination-bake, the wafer was exposed again using the second layer

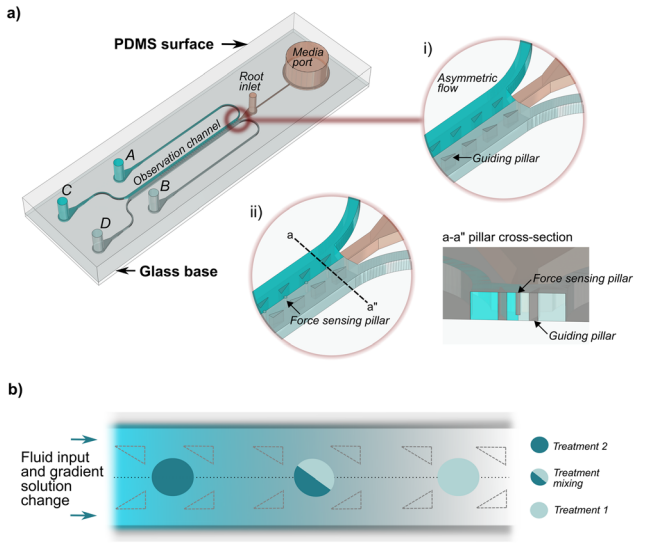

Fig. 1 Bi-dfRC equipped with asymmetric flow capabilities, displaceable micropillars, and controlled solution change delivered *via* the multiplexed media delivery system (MMDS). (a) Schematic diagram depicting the bi-dfRC microchannel with asymmetric flow achieved using a steady flow input (asymmetric non-mixing treatments displayed as dark and light blue). The bi-dfRC pillar array design variation shown in i) and ii) depict where the pillars sit in relation to the triangular guidance array. The a–a pillar cross section shows the free-moving ability of the pillars. (b) Gradient asymmetric treatment introduction in the observation channel, following solution change under a steady flow rate. Treatment one (light blue) is replaced by treatment two (dark blue) over time with mixing in the microchannel, resulting in a gradual concentration build-up of treatment two over time.

photomask at an exposure dose of 1100 mJ cm^{-2}. Followed by the PEB and development in PGMEA, the final master mold was completed *via* a ramped hard-bake.

To prevent elastomer sticking, an anti-adhesion agent (trichloro(1*H*,1*H*,2*H*,2*H*-perfluorooctyl)silane, Sigma-Aldrich) was applied to the mold using a vacuum desiccator. This step was repeated following 5 uses of the wafer as a mold master. For replica-molding, a polydimethylsiloxane (PDMS) silicone pre-polymer (Sylgard 184, Electropar) was prepared by mixing base and curing agent in a 10 : 1 w/w ratio, casting this onto the wafer mold and degassing. Next, the set-up was cured on a hotplate for 2 h at 80 °C. PDMS was then removed from the mold, subsequently baked for another 2 h, then inlet and outlet holes punched.

PDMS containing the bi-dfRC negative was O_2-plasma activated (PIE Scientific Tergeo) and bonded to glass microscope slides, followed by further baking for 2 h to strengthen the bond to the substrates. Finally, a polyvinylpyrrolidone (PVP) solution was pipetted into the microchannels for at least 1 minute for hydrophilic surface retention, followed by washing and drying.

2.2 Adaptable MMDS with tubing configurations

Two variations of multiplexed media delivery systems (MMDS) were designed: MMDS1, optimised for treatment switching with directional flow alteration, and MMDS2, designed for fast treatment changes (Fig. 2). Both configurations utilised two distinct flow paths to deliver separate treatments into the bi-dfRC. The initial MMDS1 configuration comprised four manual switching valves (HPLC) and eight Low-Pressure Unions (P-702, Kinesis). These components were interconnected by 757 mm of tetrafluoroethylene (ETFE) tubing (OD 1/16″, Kinesis, 1517 L) with Flangeless Fittings (1/4-28, Kinesis, XP-235x) and Quick Connect Luer Adapters (Kinesis, P-628). Stainless steel 90° bent couplers (Darwin Microfluidics, PN-BEN-18G-20) and platinum-cured silicon sleeves (Darwin Microfluidics, SHE-TUB-SIL-1 × 1) primed the ends of the tubing. In MMDS2, the system was simplified by reducing tubing length to 434 mm and featuring only two manual switching valves. All components were arranged on a custom flow-matrix mount.[33] Active pumping of multi-syringe-injected solutions was achieved using a programmable syringe pump (PHD2000 70-2001, Harvard Apparatus).

2.3 Media preparation

All plant culture media were sterilised by autoclaving at 121 °C for an hour. Agarose plates were prepared to a final concentration of half-strength liquid Murashige and Skoog

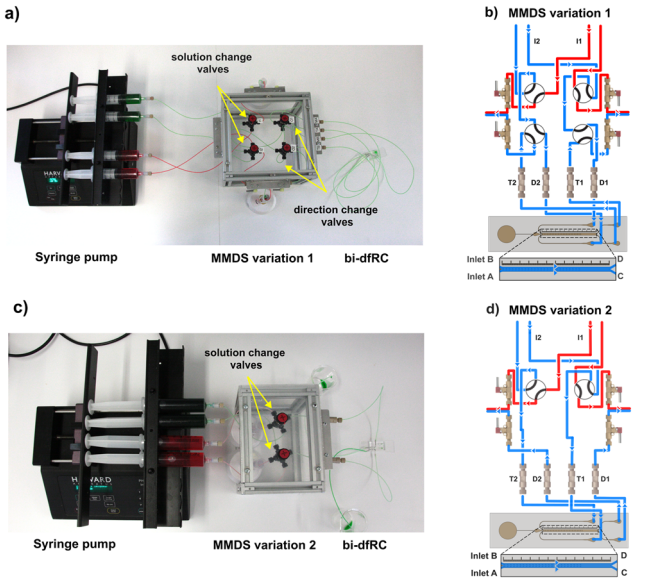

Fig. 2 MMDS variations for the delivery of treatments following solution and/or directional change into the bi-dfRC microchannel. Low-Pressure Unions are labelled T1–T2 and D1–D2. (a) Syringe pump and MMDS variation 1 for delivery of test solutions into the bi-dfRC microchannels, harboring solution and directional change manual switching valves set to deliver full treatment (green) at the shoot site (differentiation zone). (b) Schematic diagram depicting the MMDS1 tubing array and the flow path for the application of a full treatment one (blue) through inlets A & B of the bi-dfRC at the shoot site. (c) Syringe pump and MMDS variation 2 for delivery of test solutions into the bi-dfRC microchannels, equipped with a single pair of solution change manual switching valves set to deliver full treatment (green) at the shoot site. (d) Schematic diagram depicting the MMDS2 tubing array and the flow path for the application of a full treatment one (blue) through inlets A & B of the bi-dfRC at the shoot site.

(1/2 MS), 0.31 mM 2-(*N*-morpholino)ethanesulfonic acid (MES), and 1% plant agarose (Duchefa Biochemie) in purified water (MilliQ), adjusting the pH to 5.6. All solutions used for plant treatment or staining on the chip were prepared in 1/2 MS/0.31 mM MES media. For fluorescence solution tracking 8-hydroxypyrene-1,3,6-trisulfonic acid (HPTS) (ab14543, Abcam) was added to a final concentration of 0.01 mM.

2.4 Seed sterilisation and culture on agarose plates

The plant lines used in this study included wild-type *A. thaliana* Col-0, transgenic G-CaMP3,[34] and Orp1_roGFP,[35] as well as wild-type *N. benthamiana*, and *S. lycopersicum*. Approximately 50 *A. thaliana* seeds were pre-sterilisated for each experiment in 1 mL of 0.1% Triton X-100 for 4 min, followed by ethanol (EtOH) for 2 min.[18] For larger or rough-surfaced seeds like *S. lycopersicum* or *N. benthamiana*, a solution containing 30% bleach was used for 10 min. After washing with sterile water, the seeds were stored at 4 °C for 12 hours for vernalisation. To initiate seedling growth, pre-sterilised seeds were placed on 1/2 MS/0.31 mM MES agarose plates. Plates were incubated vertically in climate-controlled growth chambers (AraLab) in short-day conditions (8 h light, 16 h dark) at 65% humidity and 150 μmol s^{-1} m^{-2} per μA light intensity for a 4-day period to facilitate seedling development.[33]

2.5 Plantlet sub-culture on-chip

Bi-dfRCs were sterilised by autoclaving at 121 °C for 1 h. Microchannels were then filled with control 1/2 MS/0.31 mM MES growth media. A small agarose square was positioned next to the bi-dfRC root inlet, and 4-day old plantlets were transferred directly into the inlet. Sub-cultured bi-dfRC devices were placed in plastic single-well plates (Nunc™ OmniTray™) with 10 mL of sterile water, then sealed with micropore tape. Plates were incubated in short-day conditions as described in section 2.4, for 3–5 days.

2.6 Propidium iodide staining on-chip

To stain plant cell walls, roots were exposed to a 100 μM PI in control (1/2 MS/0.31 mM MES) media for 10 min in the dark, then washed with control media. The stain was injected into the bi-dfRC microchannels through the tip site inlets. Samples were imaged using fluorescence microscopy to assess cell viability and growth, specifically to determine the localisation of propidium iodide (PI) within the cell wall or nucleus.

2.7 Zoospore introduction on-chip

To produce *P. capsici* zoospores, a mycelium culture of strain 1534 expressing the tandem dimer fluorescent protein (tdTomato) was grown on V8 agar (Unclarified, 10%) with antibiotics (carbenicillin 50 mg mL^{-1}, vancomycin 25 mg mL^{-1}, and geneticin 50 mg mL^{-1}) for 1–2 weeks at room temperature in the dark.[36] Using sterile technique, mycelium plugs were placed mycelium-side-down onto fresh V8 agar without antibiotics. Plates were then incubated under lights for 7–10 days. To induce zoospore release from mature sporangia, 5 mL of ice-cold water was added to a single plate. The sporangia were dislodged from the mycelium using a glass spreader, and the mixture was decanted into a 15 mL Falcon tube. The suspension was immediately placed under light for 40 min, followed by a cold shock at 4 °C for 10 min. After, the suspension was incubated with light for 5 min then zoospore release was observed every 5 min until a sufficient quantity was obtained (approximately 100 motile zoospores within the field of view of the eyepiece). Cell suspensions containing motile zoospores were then passively injected into the bi-dfRC microchannel using a pipette.

2.8 Fluorescence microscopy

Experiments were conducted using an epifluorescence microscope (Zeiss, AX10) with a 5× lens (EC Plan-Neofluar 5×/0.15 M27). Green fluorescence was detected using an eGFP filter (EX450 nm/EM590 nm), and red fluorescence was detected using an mRFP1.2 filter (EX590 nm/EM612 nm). The light source (HXP 120 V) was set to 50% for all fluorescent filters. Bright field (BF) was adjusted to 30% with a TL lamp, and a 2.7 ms exposure time was used. For experiments using *P. capsici* zoospores, samples were captured using a fluorescent microscope (Leica CTR6000) with a 5× lens (HC PL FLUOTAR/0.15), using multi channels: bright field (exposure = 1.03), GFP-LP (exposure = 500), orange (exposure = 500).

2.9 Data analysis

Videos and images were analysed using the Fiji version of ImageJ software (v2.9.0/1.53t).[37] Signal analysis involved selecting three vertical regions of interest (ROIs) (maturation/elongation, elongation/differentiation, and tip zones) and three horizontal ROIs (cortex 1, stele, and cortex 2). For growth rate analysis, the velocity measurement and segmented line tool were used to track root tip movement. Force sensing analysis utilised Pillar Centroid Tracker software.[38] Fluorescent intensity readings were gathered using the ImageJ measure tool. Zoospore tracking and velocity measurements were conducted in Fiji using TrackMate[39,40] and MTrackJ,[41] respectively. Fluorescence data were collected using the linear or freehand selection tools. Fluorescence intensity data for *P. capsici* treated replicates were plotted as the average fluorescence intensity, calculated using $\Delta F/F = (F - F_0)/F_0$, where F_0 represents time point 0. Data analysis involved two-tailed paired *t*-tests (95% confidence level, $P < 0.05$). All videos were edited in ZEISS ZEN, exported as AVI uncompressed, and set to different fps for presentation purposes only. Videos and images were brightened for presentation, but not for quantification (GFP filter brightness; 7500, RFP filter brightness; 4500).

3 Results and discussion

Previous studies have shown that roots primarily respond to a sudden exposure to osmotic stress with a strong Ca^{2+} burst that exhibited a wave-like pattern emanating from the stress site.[15,16,18] This research introduces a novel approach for studying signal responses, using a microfluidic method with a valve-controlled multiplexed media delivery system (MMDS). Unlike traditional methods whereby treatments are introduced at fixed concentrations (usually maximum concentration), this new method allows for finely controlled switching of treatment gradients within the bi-dfRC microchannel. Hence, concentration gradients can be applied, mimicking the fluctuating conditions that plants are exposed to in the natural environment. This study presents a customisable bi-dfRC microfluidic device for observing root growth in various plant species under salinity stress.[33] For the first time, the bi-dfRC included displaceable micropillars to study root growth and signalling responses to force sensing. Signal analysis was only performed on *A. thaliana* roots, due to the lack of suitable transgenic detector lines in other species.

3.1 Multiplexed media delivery systems for fluidic control

Optimising media introduction in microfluidic studies has led to significant advances in precise fluid manipulation and delivery.[42] Previous mammalian research used a placenta-on-a-chip device with external rocking to simulate dynamic cell culture conditions and passively modify treatment mixing.[43] In a recent plant study, root signalling responses were observed by actively controlling steady asymmetric flow with a syringe pump.[16,28] Sample delivery methods affect treatment mixing, resulting in either gradual or rapid concentration changes over time.[44,45] The newly developed MMDSs allow for flexible treatment changes during imaging, which creates a longitudinal gradient front in microchannels (Fig. 1). Constructed with precision tubing and valve components, the two MMDS variations establish separate circuits, maintaining asymmetric flow (Fig. 2). MMDS1, equipped with four manual switching valves, controls treatment changes and flow direction within the bi-dfRC microchannel (Fig. 2(a and b)). In contrast, MMDS2 lacks directional change valves (Fig. 2(c and d)), offering faster treatment switching but without flow direction capabilities.

Simultaneously switching solution valves enables complete media introduction (Fig. 2(b and d), S1(a–c) and S2(a–c)†), whereas switching one valve results in asymmetric media introduction (Fig. S1(d and e) and S2(d and e)†). This principle similarly applies to the directional change valves in MMDS1 (Fig. S1†). Colored dyes were injected into the bi-dfRC to track gradient introduction after solution switching. MMDS1 required ~30 min for a gradient treatment switch in the bi-dfRC microchannel, whereas MMDS2 achieved the same in ~4 min, representing a ~7.5-fold reduction in delivery time (Video S1†). To achieve this, the length of tubing in MMDS2 was decreased from 757 mm to 434 mm, and the inner diameter (ID) reduced from 1.02 mm to 0.5 mm. In this research, all experiments used MMDS1 with only treatment switching valves operated. Future research could explore altering flow direction and faster solution changes using MMDS1 and MMDS2, respectively.

3.2 *A. thaliana* root signalling responses towards salinity accumulation and *P. capsici* zoospores

During osmotic stress and pathogen attack, plants activate primary defence responses including early Ca^{2+} signalling.[46] A previous study using the genetically encoded Ca^{2+} indicator (GECI) R-GECO1 in controlled microfluidic systems showed that osmotic stress and the pathogen peptide flagellin22 (flg22) induced a signal in cells and tissues in direct contact with the stressor.[16] Recently, directional systemic Ca^{2+} signals (root-shoot, traverse, shoot-root) were observed upon exposure to 100 mM NaCl, depending on treatment localisation at the root differentiation zone or tip.[18] Localisation and intensity of the signal is treatment-specific and orientation-dependent.[15,16,32]

Novel results reported here highlight that salinity stress induced a concentration dependent Ca^{2+} signal (Fig. 3). This was observed by creating a longer gradient front between treatments, *via* real-time solution change, tracked with HPTS dye using the MMDS1, and precisely timing the upregulation of the Ca^{2+} signal relative to the gradient front. Prior to adding the dye, the microchannel containing the root was flushed with control treatment to adapt the root to a consistent flow. Movies of wild type Col-0 and transgenic G-CaMP3 roots treated under control conditions are available in the ESI† (Video S2). HPTS dye did not cause significant auto-fluorescence or induce a Ca^{2+} response, making it suitable for tracking solution change timing during fluorescence imaging (Fig. 3(a and b) and S3(a and b); Video S2†).

Interestingly, weak Ca^{2+} flickering occurred for 30 s within stele tissue of the *A. thaliana* primary root as the concentration of NaCl increased up to 100 mM on both sides of the observation channel (Fig. 3(c and d) and S3(c); Video S2†). Next, a strong concentration-dependent Ca^{2+} burst initiated within all cells of the epidermis and cortical tissues of the elongation and maturation/differentiation zone (P-value = 0.04), dispersing tip-ward at an average speed of 16.67 ± 0.5 μm s^{-1} throughout the stele tissue over 5 min, before gradually dissipating (P-value = 0.3). Fluorescence intensity of the signal increased to an average of 3000 (gray-scale) after treatment with NaCl (Fig. 3(c and d)). In a prior study we showed that a non-linear solute change triggered a more intense fluorescence increase reaching an average of 4500 after treatment with NaCl and a faster signal dispersion of 6.8 μm s^{-1}.[18] Temporal dynamics suggest that a sudden stress triggers an immediate and more intense response, whereas gradual stress introduction results in a more prolonged, moderate response.

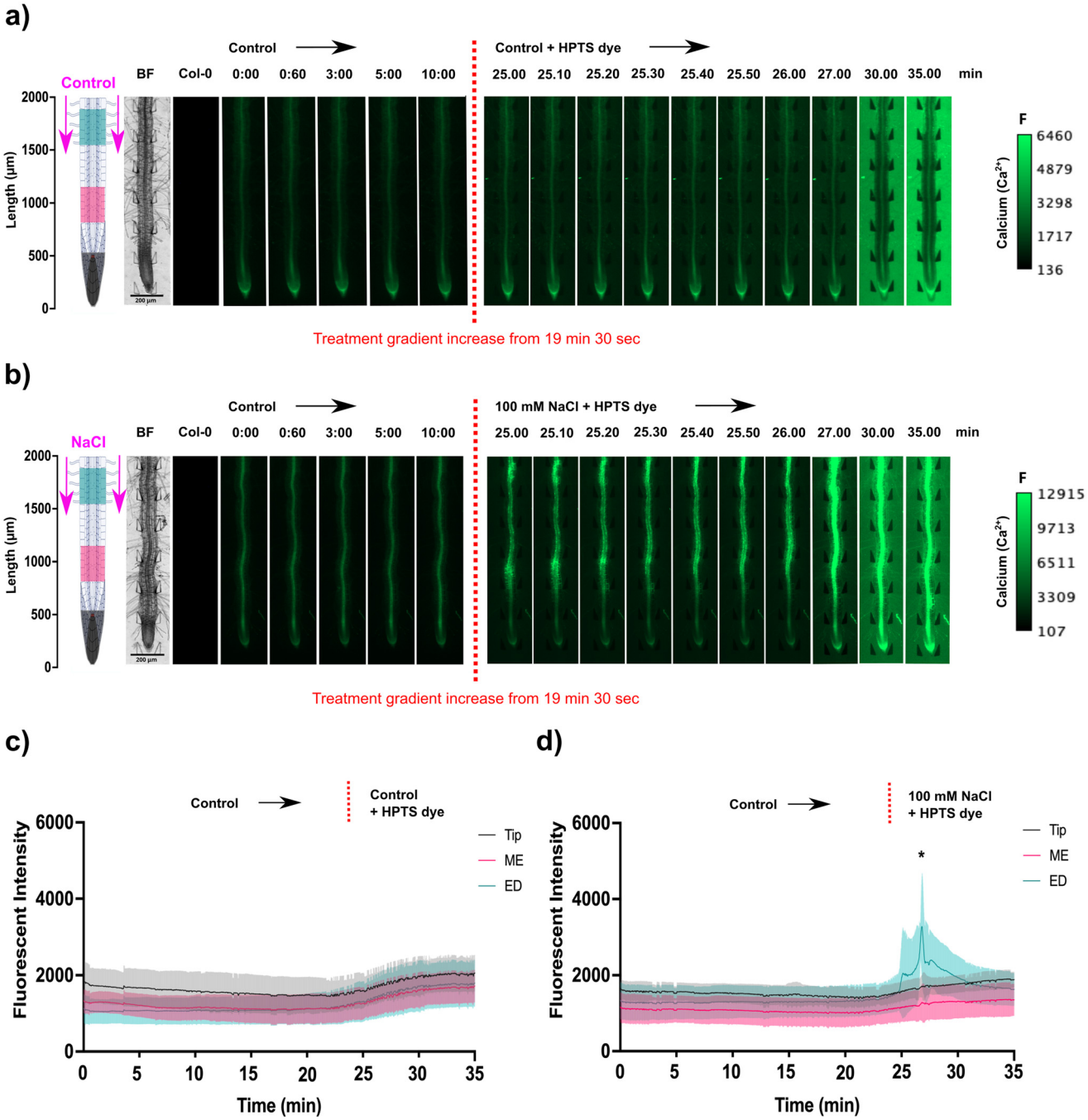

Fig. 3 Spatiotemporal localisation of Ca^{2+} signals in *A. thaliana* G-CaMP3 roots upon salinity accumulation. Flow rate was set to 20 µL min^{-1}. Original video files are 1 fps. Control media (1/2 MS/0.31 mM MES) was injected into the bi-dfRC microchannel through inlets A & B (at the shoot site) to create a steady flow for ~19 minutes, then switched to the desired experimental treatment using a gradient. The gradient was tracked by fluorescence using 0.01 mM HPTS dye (green). All root schematics depict treatment application with the rectangular regions of interest highlighted (refer to key). Bright field (BF) and control (wild type Col-0) roots are displayed on the left of the figure. Scale; *F* = fluorescence intensity. (a) Following treatment switch to control media, no Ca^{2+} burst indicated by the G-CaMP3 was observed (n = 3). (b) Following switch to 100 mM NaCl, a strong Ca^{2+} signal was detected (n = 3). (c) Line graph with a two-way ANOVA multiple comparisons Tukey's honestly significant difference (HSD) mean comparison test (P-value ≤ 0.05) depicting average fluorescence intensity (grey scale; pixel brightness) of G-CaMP3 within three rectangular regions of interest (tip, maturation/elongation (ME) zone and elongation/differentiation (ED) zone) upon targeted exposure to control treatment (n = 3). (d) Line graph depicting average fluorescence intensity of G-CaMP3 across three rectangular regions upon NaCl treatment (n = 3). Asterisks (*) indicate statistical significance.

In the microfluidic system setup, a novel observation was made during PI staining of *A. thaliana* root cell walls. Under standard control conditions, PI traveled through the xylem, moving towards the shoot within 2 hours (Fig. 4(a), S4(b) and S5(a and c); Video S3†). However, under 100 mM NaCl-induced salinity stress, while PI still

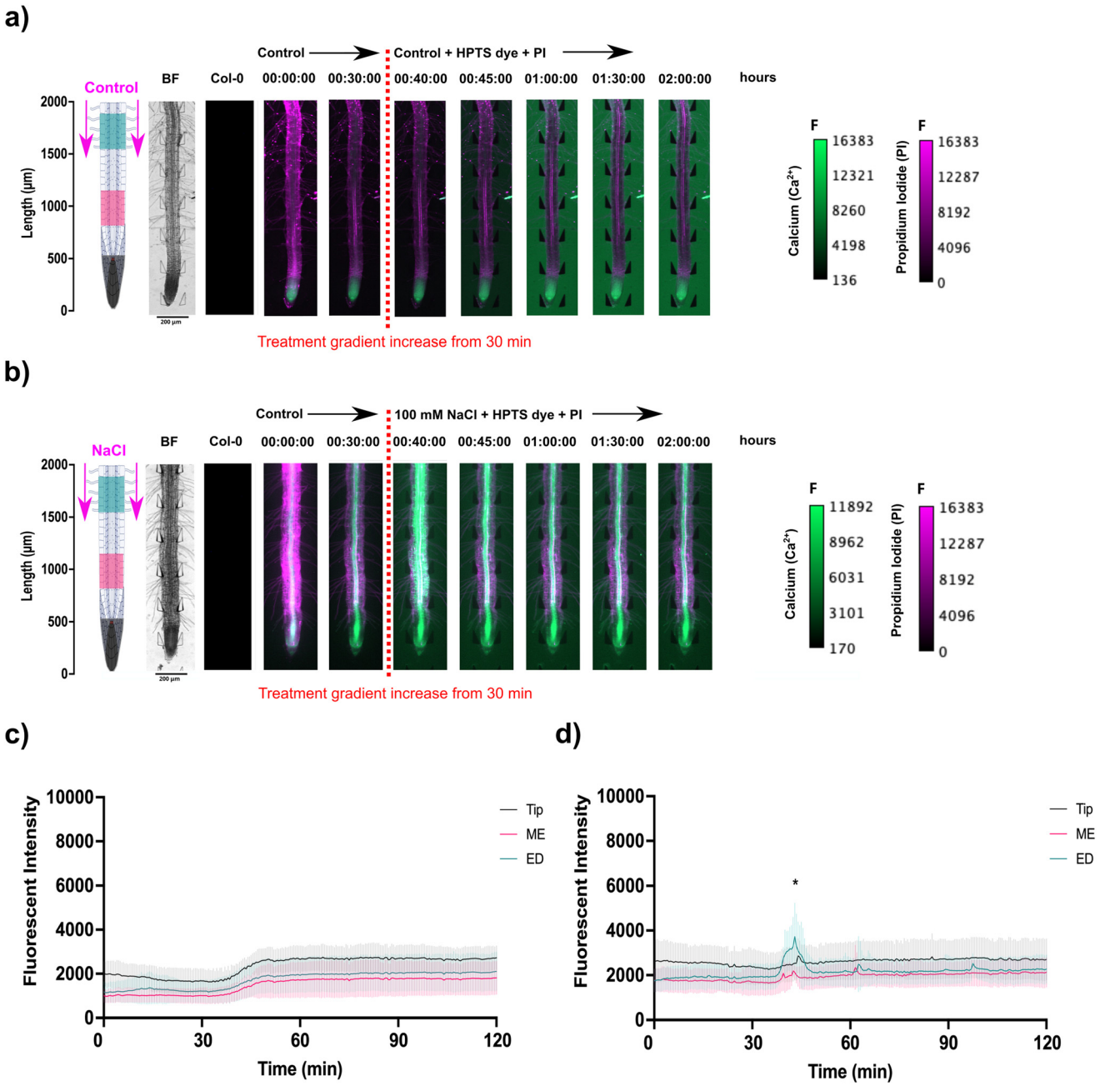

Fig. 4 Propidium iodide (PI) staining of *A. thaliana* G-CaMP3 roots and the resulting spatiotemporal localisation of fluorescence following solution change through inlets A & B at the shoot site. The continuous flow (20 µL min^{-1}) of control media (1/2 MS/0.31 mM MES) was maintained for 30 minutes. Original video files are 0.05 fps. Solution change caused the gradient shown for control and 100 mM NaCl for 2 hours. Root schematics on the left depict treatment application (magenta arrows) and the rectangular regions of interest (refer to key). The bright field (BF) channel and control (wild type Col-0) roots are displayed adjacently (scale; *F* = fluorescence intensity). (a) Under control conditions, PI stain (RFP; magenta) was transported shoot-wards through the xylem over 2 hours, following the treatment switch to control media supplemented with HPTS dye (*n* = 3). No Ca^{2+} burst indicated by the G-CaMP3 is observed. (b) During salinity stress, the PI fluorescence indicated reduced transported through the xylem and phloem over 2 hours after the introduction of 100 mM NaCl supplemented with HPTS dye (*n* = 4). The Ca^{2+} burst indicated by the G-CaMP3 was observed upon 100 mM NaCl introduction at approximately 37 minutes. (c) Line graph with two-way ANOVA multiple comparisons Tukey's honestly significant difference (HSD) mean comparison test (*P*-value ≤ 0.05) depicting average fluorescence intensity (grey scale; pixel brightness) of G-CaMP3 within three rectangular regions of interest (tip, maturation/elongation (ME) zone and elongation/differentiation (ED) zone) upon targeted exposure of control treatment for a duration of 2 hours (*n* = 3). (d) Line graph depicting average fluorescence intensity of G-CaMP3 across three rectangular regions upon the solution change to 100 mM NaCl treatment for a duration of 2 hours (*n* = 4). All experiments used a concentration of 0.01 mM HPTS dye (green). Asterisks (*) indicate statistical significance.

entered the xylem, its movement was reduced (Fig. 4(b), S4(d) and S5(b and d); Video S3†). Stresses in the vascular tissue have long been known to induce occlusions (of different compositions) and can restrict xylem and phloem

flow, impacting water status and carbohydrate movement.[3] This observation suggests PI can be used in future research as a tool to track flow in the xylem under various treatment conditions. Multiple localised Ca^{2+} bursts were also observed throughout the stele tissue of the root, continuing for 1.5 h following initial upregulation (Video S3†). This suggests that Ca^{2+} signalling under salt stress involves encoding information through repeated oscillations to maintain overall Ca^{2+} homeostasis for a prolonged signalling response.

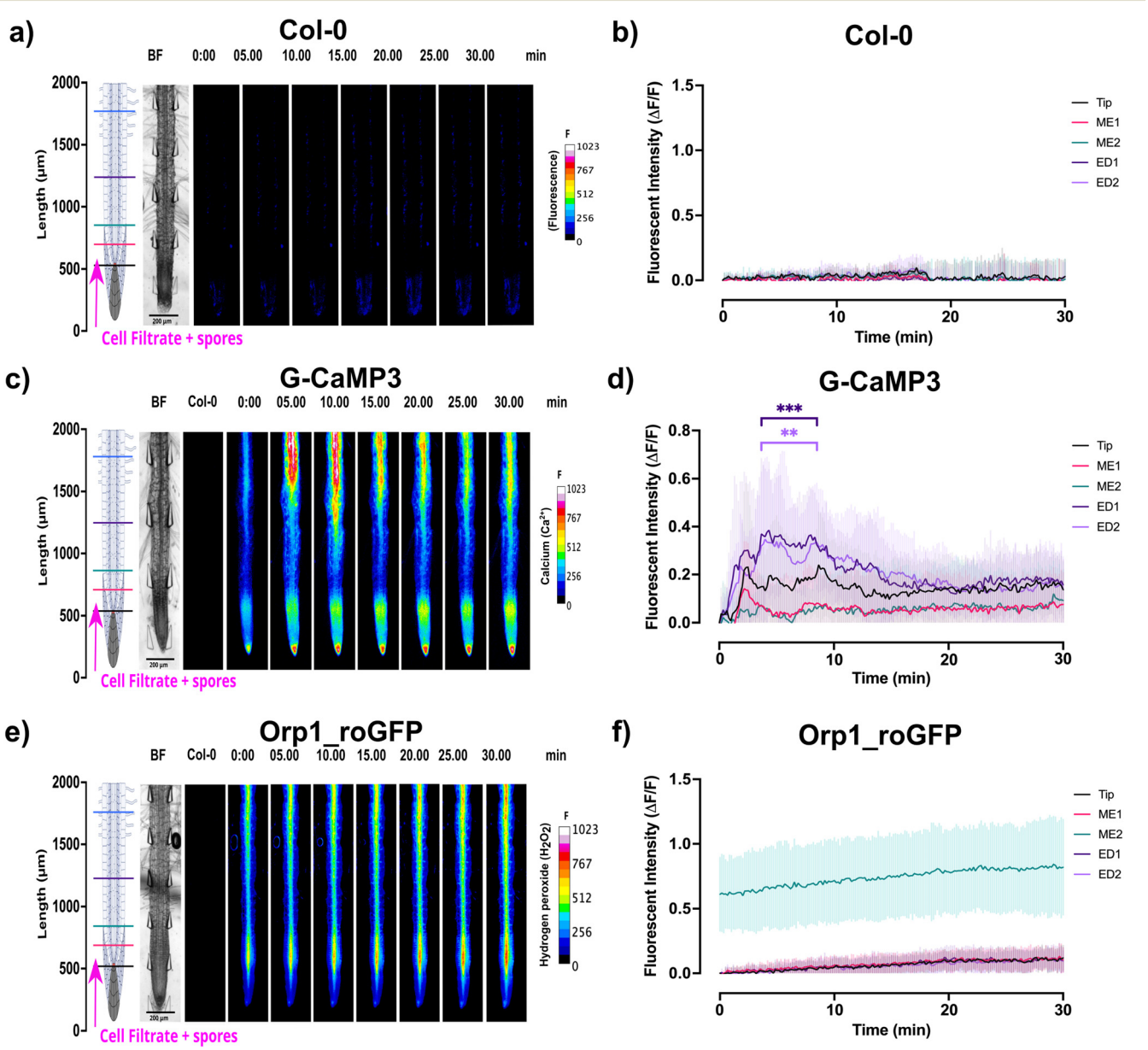

Fig. 5 Signal analysis (indicating Ca^{2+} and H_2O_2) in *A. thaliana* roots following passive injection of *P. capsici* cell suspension and zoospores at the root-site (inlet C) of the bi-dfRC. Root schematics located on the left show treatment application (magenta arrows) and linear sections highlighted (refer to key). Bright field (BF) channel is displayed adjacently. Heat maps were brightened for display purposes (scale; *F* = fluorescence intensity). All line graphs depict normalised ($\Delta F/F$) fluorescence intensity (grey scale; pixel brightness) across 5 linear sections (tip, ME1, ME2, ED1 & ED2) with a two-tailed paired *t*-test (*P*-value ≤ 0.05) with a 95% confidence interval. Original video files are 0.2 fps. (a) Heat map depicting no signal release in Col-0 upon pathogen cell suspension treatment at the root-site of the bi-dfRC ($n = 6$). Spore localisation was observed in six replicates. (b) Line graph depicting no fluorescent accumulation in Col-0 roots upon targeted exposure of pathogen treatment at the root-site of the bi-dfRC ($n = 6$). (c) Heat map depicting a strong Ca^{2+} burst indicated by the G-CaMP3 within 5 s, following pathogen treatment through the root-site (inlet C) of the bi-dfRC ($n = 8$). Spore localisation was observed in four replicates. (d) Line graph depicting a Ca^{2+} burst indicated by the G-CaMP3 upon targeted exposure of pathogen treatment at the root-site of the bi-dfRC ($n = 8$). (e) Heat map depicting a gradual H_2O_2 release, indicated by the Orp1_roGFP fluorescence over 30 min following pathogen treatment at the root-site of the bi-dfRC ($n = 9$). Spore localisation was observed in five replicates. (f) Line graph depicting H_2O_2 accumulation indicated by Orp1_roGFP fluorescence upon targeted exposure of pathogen treatment at the root-site of the bi-dfRC ($n = 9$).

Ca^{2+} signalling in response to the passive injection of *P. capsici* zoospores into the bi-dfRC microchannel at the tip site was also documented. Results showed that the Ca^{2+} signal indicated by the G-CaMP3 was rapidly detected during early pathogen recognition, originating from epidermal cells at the tip, maturation, elongation and differentiation zones within seconds (Fig. 5(a and b) and S6, Video S4†). The signal then traversed to the stele tissue of the elongation/differentiation zones, followed by a vertical bi-directional (shoot-root and root-shoot) signal throughout the stele tissue, over the next 10 min (Fig. 5(a and b) and S6, Video S4†). Additionally, signal from the Orp1_roGFP fluorescent H_2O_2 reporter gradually increased, predominantly in the stele tissue of the elongation and maturation zones, over 30 min (Fig. 5(c and d) and S6, Video S4†). Interestingly, 24 h post-infection, whole-root Ca^{2+} and H_2O_2 levels remained high, in addition to observed root swelling (Fig. 6(b and c) and S6(b, c, e and f); Video S4†). The initial Ca^{2+} burst could serve as a warning, initiating secondary responses including the hypersensitive response (HR).[47] Moreover, cells at the site of infection experience alterations to ion concentrations, ROS generation and defence gene activation, leading to programmed cell death.[48] Maintaining low cytosolic levels of Ca^{2+} is vital to prevent damage. Prolonged increased cytosolic Ca^{2+} levels have been associated with apoptosis and effector triggered immunity.[49]

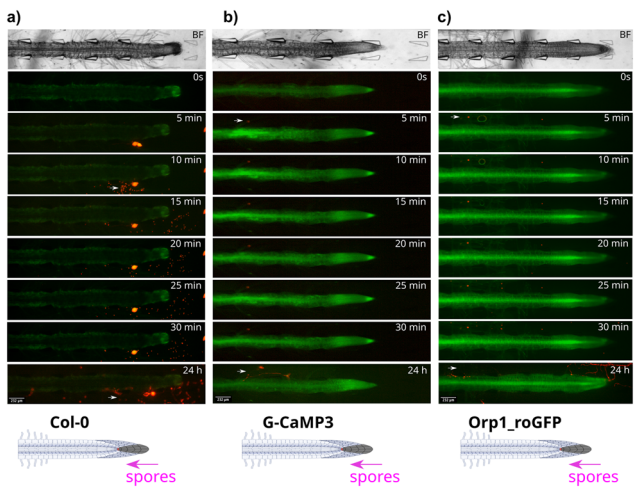

Fig. 6 *P. capsici* zoospore localisation patterns in wild type Col-0 and transgenic G-CaMP3 and Orp1_roGFP *A. thaliana* roots. Pathogen spores were passively injected through the tip-site of the bi-dfRC (inlet C), over 24 h. Bright field (BF) channel displayed above. Schematic diagrams depicting treatment application (white arrow) displayed below. Key events including zoospore localisation, germination and protrusion into root tissue are highlighted with magenta arrows. Original video files are 0.2 fps. (a) Zoospore release from a sporangium situated below a Col-0 primary root, within the bi-dfRC microchannel. Zoospores localise to the root tip and maturation/elongation (ME) zone over 30 min. Infection is observed at the elongation/differentiation zone (ED) of the primary root after 24 h. No root signalling was observed. (b) Zoospore localisation to a G-CaMP3 root hair within 5 min. A strong Ca^{2+} burst indicated by the G-CaMP3 was observed within 5 min following active injection of zoospores, persisting for 30 min. Infection at the ED zone was observed 24 hours following exposure. Whole root Ca^{2+} levels remain elevated 24 h following infection. (c) Zoospores localise to Orp1_roGFP root hairs, ME and ED zones within 5 min. A gradual increase in H_2O_2 was observed over 30 min, following the passive injection of pathogen spores at the tip site (inlet C) of the bi-dfRC. Infection is shown at the tip and DZ of the primary root after 24 h. Whole root ROS upregulation H_2O_2 was observed 24 h following infection.

3.3 Root-oomycete interactions between *A. thaliana* and *P. capsici* zoospores

Microfluidic systems have been used to observe initial zoospore localisation patterns.[17,50–52] Recent research on *P. parasitica* behavior near *A. thaliana* roots revealed a critical threshold distance (around 300 μm) where zoospores changed behavior, indicating signal perception.[53]

Upon examining *P. capsici* zoospore distribution following passive injection at the bi-dfRC tip site inlet, distinct spatial preferences were also revealed. Although passive injection typically results in a more uniform distribution compared to a Poiseuille profile, it is important to note that local microenvironment factors such as root hairs and channel geometry could still influence the observed variations in zoospore velocities. Results revealed zoospore localisation at root hairs and epidermal cells within the maturation zone (Fig. 6 and S5, Video S4†), in addition to the area of elongation. In a prior study, a similar microfluidic set-up observed *P. parasitica* localisation at the root tip.[53] The difference in zoospore attachment sites suggests varied host recognition mechanisms or colonisation strategies.[54] The study also documented velocity and directionality changes of the zoospore upon movement towards the root.[53] Here, the velocity of the zoospores significantly varied over 30 min, ranging from a minimum of 4.5 ± 10 μm s^{-1} in close proximity to the root or root hairs to a maximum speed of 172 ± 93 μm s^{-1} while swimming towards the root (Fig. S6(g)†), suggesting a dynamic relationship between the root environment and zoospore movement.

Zoospores encysted and germinated within 24 h, directly infecting epidermal cells in the elongation and differentiation zones (Fig. 6(a and c)). Infection may also occur through the root hairs (Fig. 6(b)), however, further studies are required to confirm this observation. The ability to infect at multiple sites offers alternative entry points, potentially enhancing overall infectibility and spread within the plant. The preference for infecting specific root zones could be influenced by factors including suberisation, nutrient availability, cell wall defence, cellular activity, or structure.

3.4 Ca^{2+} signalling and growth responses upon contact with displaceable obstacles

The protrusive forces of tip-growing organisms, especially the single-celled tips of fungal oomycete hyphae, such as *Achlya bisexualis* have been tracked using displaceable micropillars in microfluidic channels,[52,55,56] an approach based on a

system originally developed to measure the multi-point locomotive forces exerted by *Caenorhabditis elegans*.[57,58] Here, the same measurement principle and force sensing pillars were used to analyse the force exerted by multi-celled plant primary root tips, also known as root growth force or root tip pressure. For this, the root force was calculated from

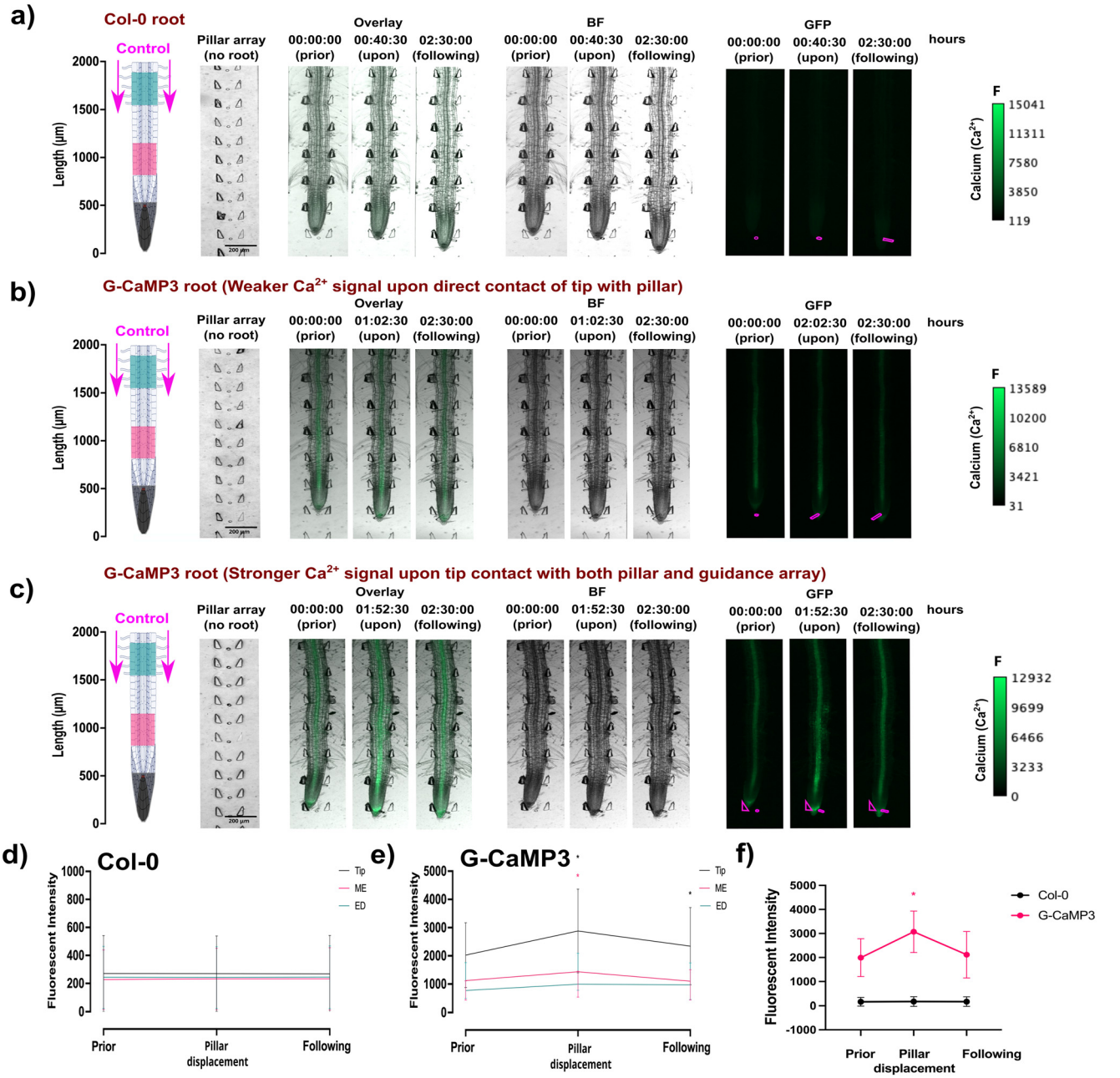

Fig. 7 The spatiotemporal localisation of Ca^{2+} signals in both *A. thaliana* wild type Col-0 and transgenic G-CaMP3 roots was observed at the tip before, during, and after touch stress for 2.5 hours. Displayed on the left are root schematics depicting control (1/2 MS/0.31 mM MES) treatment application (magenta arrows) with rectangular regions of interest highlighted (refer to key). Bright field (BF) with the pillar array in the absence of a root is displayed adjacently (scale; *F* = fluorescence intensity), followed by an overlay of the BF and GFP channel. Pillars are overlayed in the GFP channel for display purposes (magenta lines). Line graphs depict normalised ($\Delta F/F$) fluorescence intensity (grey scale; pixel brightness) across linear sections or the root tip with a two-tailed paired *t*-test (*P*-value ≤ 0.05) with a 95% confidence interval. Original video files are 0.1 fps. (a) A Col-0 root depicting no fluorescence increase upon root tip contact with a displaceable micropillar. (b) A G-CaMP3 root depicting a non-directional localised Ca^{2+} release indicated by the G-CaMP3 at the tip and elongation zone upon root tip contact with a displaceable micropillar at approximately 2 hours. (c) A G-CaMP3 root depicting a strong directional Ca^{2+} release indicated by the G-CaMP3 at the tip, elongation zone and differentiation zone after root tip contact with both the displaceable micropillar and guidance array at approximately 1 hour 52 minutes. (d) Line graph showing the average fluorescence intensity in Col-0 roots within three rectangular regions of interest (tip, maturation/elongation (ME) zone and elongation/differentiation (ED) zone) upon force sensing at the tip (n = 5). (e) Line graph showing the average fluorescence intensity of G-CaMP3 within three rectangular regions of interest upon force sensing at the tip (n = 5). (f) Line graph showing the average fluorescence intensity at the root tip in Col-0 and G-CaMP3 plants (n = 5).

micropillar deflection following a spring-like mechanical model which combines pillar bending and shear.[56,57] Plants respond to mechanical stress through various molecular and physiological mechanisms, impacting growth, development, and cell wall modifications.[59] Upon pillar displacement, both *A. thaliana* Col-0 and G-CaMP3 roots showed a significant increase in average growth force, from 5.1 ± 1.6 to 88 μN ± 39 and from 6 ± 1.2 to 102 μN ± 14.2, respectively (Fig. S7 and Video S5†).

When subjected to touch, pressure, or gravity, plants alter intra-cellular Ca^{2+} levels.[60] Early studies with Ca^{2+}-sensitive probes including aequorin in *A. thaliana* showed rapid intracellular Ca^{2+} spikes in response to touch stimuli, especially in cotyledons.[61] Recent research also noted Ca^{2+} waves in cotyledons following touch stress.[62] In roots, using the FRET-based Ca^{2+} sensor YC3.6, localised Ca^{2+} bursts were shown to occur in stimulated cells in the cytoplasm and nucleus within seconds and rapidly dissipate.[63] Despite extensive understanding of plant responses to mechanical stress, none of these studies reported the force of root contact.

In this study, flexible micropillars within the bi-dfRCs microchannel were used for the first time to measure the root contact force required to initiate a stress response. Results revealed that a weak non-directional Ca^{2+} signal was observed in the stele tissue of the maturation/elongation zone in response to a root growth force of 34 μN (Fig. 7(b) and S7(a); Video S5†). Conversely, when a G-CamP3-labeled root tip encountered both the displaceable micropillar and root guidance array simultaneously, a stronger directional (shoot-ward) Ca^{2+} signal was observed through the stele tissue in response to an increased root growth force of 85 μN over 10 min. The initiation, propagation, and intensity of the touch-induced Ca^{2+} burst depended on the force exerted by the root's multiple cells to overcome the micropillar obstacle and continue growing.

Interestingly, the Ca^{2+} upregulation was observed at the elongation/differentiation zone of the primary root, not the root tip itself (Fig. 7(c) and S7(b); Video S5†). Additionally, the Ca^{2+} signal initiation did not occur upon initial contact of the root tip cells with the pillar, but instead 1–1.5 hours later as the root pushed past the obstacles. These findings suggest that root growth force is linked to Ca^{2+} signalling. This highlights the potential importance of incorporating soil-like structures on-chip, as they may influence root behavior in ways that are relevant to certain measurements.[21]

3.5 Root growth response to solute concentration accumulation in various plant species

Plants adjust their root structure in response to stress to improve resource uptake and to cope with challenging conditions.[64] Previous research found that prolonged salt and drought stress can reduce plant growth due to increased water loss through open stomata and cell shrinkage.[7,65–67] In natural soil conditions, *A. thaliana* roots typically grow at rates ranging from 55 to 120 μm h^{-1}.[68] Here, the growth rates of *A. thaliana*, *N. benthamiana*, and *S. lycopersicum* plants were observed under saline accumulation. Results revealed a contrast in root growth across plant species when subjected to 1 hour control (1/2 MS/0.31 mM MES) treatment, then switched to 1-hour NaCl (100 mM) treatment. In the control medium, *A. thaliana* roots extended an average of 63.1 μm ± 44 at a velocity of 41 μm h^{-1} ± 18, facilitated by a consistent flow rate of 20 μL min^{-1} (Fig. 8(a and b) and Video S6†). When exposed to prolonged salinity stress, an average growth reduction of 32 μm ± 13 was observed with a reduced velocity of 26 μm h^{-1} ± 17 (Fig. 8(a and b) and Video S6†). Comparatively, under control conditions, *N. benthamiana* roots extended an average of 47 μm ± 25 at a velocity of 24 μm h^{-1} ± 19. Again, under salt stress, growth distance reduced to 26 μm ± 16 at a velocity of 12 μm h^{-1} ± 11 (Fig. 8(a and b) and Video S6†). This highlights the significant impact prolonged salinity has on development in smaller roots. Interestingly, under control conditions, *S. lycopersicum* roots extended an average of 102 μm ± 37 at a velocity of 59 μm h^{-1} ± 28, which increased to 196 μm ± 100 under salt stress (Fig. 8(a and b) and Video S6†). Although *S. lycopersicum* took longer to

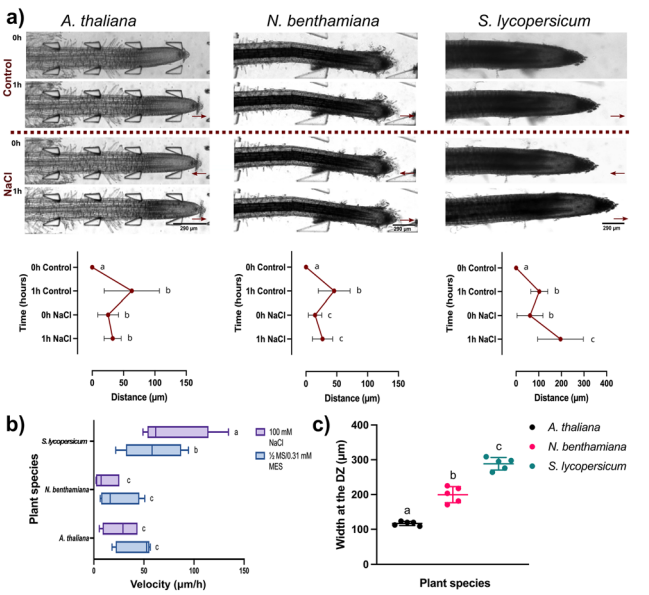

Fig. 8 Root growth analysis conducted on *A. thaliana*, *N. benthamiana* and *S. lycopersicum* under varying solute concentrations. Treatments alternated between control (1/2 MS/0.31 mM MES) and salinity stress (100 mM NaCl) using the MMDS. The growth of the same roots is shown over time in each condition. Original video files are 0.08 fps. (a) Bright field image of root growth of the three plant species after control treatment for 1 h followed by salinity treatment for 1 h (scale bar = 290 μm). The maroon line indicates the switch from control to NaCl treatment. All graphs depict paired *t*-test (two-tailed) with a confidence level of 95% ($P < 0.05$). Plots show the average root growth (μm) of the three plant species under control and salinity treatments for 1 h ($n = 5$). (b) Box and whisker plot comparing the average root velocity (μm h^{-1}) of the three species under control and salinity treatments ($n = 5$). (c) Scatter plot comparing the average root width (*W*) of the three plant species at the differentiation zone (DZ) ($n = 5$).

germinate, all plants were at the same developmental stage (seedling stage; developed a primary root and beginning to form root hairs, but secondary roots have not yet emerged) when introduced into the microfluidic channels. Measurements confirmed that *S. lycopersicum* roots were significantly thicker (*W*) at the differentiation zone (288 μm ± 18) than those of *A. thaliana* (116 μm ± 6) and *N. benthamiana* (200 μm ± 23) (Fig. 8(c)). This variation in root width was accommodated by using three different bi-dfRC dimensions to fit the varying sizes of roots.[33] Previous research using an observational system found that thicker roots with lower tissue density support water absorption and increased nonstructural carbohydrates (NSC) used for managing osmotic changes.[69] This observation may provide insight into why the larger tomato plants may have tolerated higher levels of salt compared to *A. thaliana* and *N. benthamiana*. The introduction of salinity stress also triggered osmotic stress, causing tip shrinkage. When the solution changed from control to 100 mM NaCl treatment at 1 hour, root tips rapidly retracted (Fig. 8(a and b)). The retraction spanned 15 to 25 μm, and occurred over approximately 10 min consistently across all three plant species despite their varying root sizes. This highlights the importance of fluidic control in investigating and understanding growth and development of different plant species under varying environmental conditions.

Conclusions

The replication of dynamic environmental gradients triggered observable responses in plant growth and development. This was shown by the impact of solute gradients on root physiology, signalling, and transport mechanisms, especially under high salinity conditions. Growth analysis conducted across diverse plant species, including *A. thaliana*, *N. benthamiana*, and *S. lycopersicum*, under salinity stress and in the presence of displaceable obstacles provided valuable insight into the mechanisms underlying plant resilience. We show for the first time the integration of force sensing micropillars into bi-dfRCs to monitor root extension and growth force responses. Additionally, the results from zoospore infection experiments contributed to advancing understanding of plant signalling mechanisms and interactions of plants and pathogens. The outcomes of this study have significance for fundamental research in plant biology and applied research in the agriculture sector, aimed to enhance plant resilience during changing environmental conditions.

Data availability

Data for this article, including images, videos and analysis, are available at Figshare at **https://doi.org/10.26021/canterburynz.26422216.v1**.

Author contributions

C. A., C. N. M. and V. N. conceived the project. C. A. designed and performed experiments. C. N. M. provided feedback on experimental design and data analysis. V. N. designed and prepared the bi-dfRC mask and MMDS. Y. S. designed and prepared the bi-dfRC mask for force sensing. P. C. B. provided support with experiments using *P. capsici* spores. S. C. W. assisted with *P. capsici* culture and zoospore production, and M. P. with microscopy. C. A. wrote the article with contributions from all authors. C. A., Y. S. and V. N. designed the figures. C. N. M. agrees to serve as the author responsible for contact and ensures communication.

Conflicts of interest

There are no conflicts to declare.

Acknowledgements

We thank Dr Edgar Huitema (University of Dundee, UK) for use of the tdTomato labelled strain of *P. capsici*; this work was carried out under plant health licence PH/6/2023. We acknowledge funding from the United Kingdom Biotechnology and Biological Sciences Research Council (BBSRC) (grant BB/T020164). Further, we thank Gary Turner and Linda Chen of the University of Canterbury Nanofabrication Laboratory for technical support. Funding was provided *via* a Biomolecular Interaction Centre PhD scholarship to C. A., Faculty of Science seed, Royal Society Te Apārangi Catalyst CSG-UOC1902 and Bioprotection Aotearoa funding to C. N. M, and Rutherford Discovery Fellowship RDF-19-UOC-019 and Biomolecular Interaction Centre funding to V. N.

References

1 X.-Q. Huang and N. Dudareva, *Curr. Biol.*, 2023, **33**, R473–R478.
2 M. Nawaz, J. Sun, S. Shabbir, W. A. Khattak, G. Ren, X. Nie, Y. Bo, Q. Javed, D. Du and C. Sonne, *Sci. Total Environ.*, 2023, **900**, 165832.
3 Z. Li, J. F. Harper, C. Weigand and J. Hua, *Plant Physiol.*, 2023, **191**, 2534–2550.
4 T. Tong, Q. Li, W. Jiang, G. Chen, D. Xue, F. Deng, F. Zeng and Z.-H. Chen, *Int. J. Mol. Sci.*, 2021, **22**, 12308.
5 S. Ghosh, M. Bheri, D. Bisht and G. K. Pandey, *Curr. Plant Biol.*, 2022, **29**, 100235.
6 D. R. Bergey, R. Kandel, B. K. Tyree, M. Dutt and S. A. Dhekney, *Springer Sci. Rev.*, 2014, **2**, 145–159.
7 W. Liu, R.-J. Li, T.-T. Han, W. Cai, Z.-W. Fu and Y.-T. Lu, *Plant Physiol.*, 2015, **168**, 343–356.
8 G. Lajeunesse, C. Roussin-Léveillée, S. Boutin, E. Fortin, I. Laforest-Lapointe and P. Moffett, *Nat. Commun.*, 2023, **14**, 713.
9 L. Zhang, L. Du and B. W. Poovaiah, *Plant Signaling Behav.*, 2014, **9**, e973818.
10 Q. Li, J. Wang, T. Bai, M. Zhang, Y. Jia, D. Shen, M. Zhang and D. Dou, *Mol. Plant Pathol.*, 2020, **21**, 502–511.

11 D. Qian and Y. Xiang, *Int. J. Mol. Sci.*, 2019, **20**, 1403.
12 S. Kumar, T. Jeevaraj, M. H. Yunus, S. Chakraborty and N. Chakraborty, *Plant, Cell Environ.*, 2023, **46**, 5–22.
13 Y. Zhang, D. Zhang, S. Huang, N. Ye and Y. He, *Trends Plant Sci.*, 2023, **28**, 1326–1327.
14 T. C. Xiong, E. Ronzier, F. Sanchez, C. Corratgé-faillie, C. Mazars and J.-B. Thibaud, *Front. Plant Sci.*, 2014, **5**, 43.
15 W.-G. Choi, M. Toyota, S.-H. Kim, R. Hilleary and S. Gilroy, *Proc. Natl. Acad. Sci. U. S. A.*, 2014, **111**, 6497–6502.
16 C. E. Stanley, J. Shrivastava, R. Brugman, E. Heinzelmann, D. van Swaay and G. Grossmann, *New Phytol.*, 2018, **217**, 1357–1369.
17 N. Yanagisawa, E. Kozgunova, G. Grossmann, A. Geitmann and T. Higashiyama, *Plant Cell Physiol.*, 2021, **62**, 1239–1250.
18 C. Allan, A. Tayagui, R. Hornung, V. Nock and C.-N. Meisrim-ler, *Front. Plant Sci.*, 2023, **13**, 1040117.
19 Z. Jiang, S. Zhu, R. Ye, Y. Xue, A. Chen, L. An and Z.-M. Pei, *PLoS One*, 2013, **8**, e76130.
20 S. F. Berlanda, M. Breitfeld, C. L. Dietsche and P. S. Dittrich, *Anal. Chem.*, 2021, **93**, 311–331.
21 C. E. Stanley, G. Grossmann, X. Casadevall i Solvas and A. J. deMello, *Lab Chip*, 2016, **16**, 228–241.
22 A. Sanati Nezhad, *Lab Chip*, 2014, **14**, 3262–3274.
23 M. Meier, E. M. Lucchetta and R. F. Ismagilov, *Lab Chip*, 2010, **10**, 2147–2153.
24 W. Busch, B. T. Moore, B. Martsberger, D. L. Mace, R. W. Twigg, J. Jung, I. Pruteanu-Malinici, S. J. Kennedy, G. K. Fricke, R. L. Clark, U. Ohler and P. N. Benfey, *Nat. Methods*, 2012, **9**, 1101–1106.
25 H. Jiang, Z. Xu, M. R. Aluru and L. Dong, *Lab Chip*, 2014, **14**, 1281–1293.
26 Y.-H. Park, N. Lee, G. Choi and J.-K. Park, *Lab Chip*, 2017, **17**, 3071–3077.
27 O. Siemianowski, K. R. Lind, X. Tian, M. Cain, S. Xu, B. Gana-pathysubramanian and L. Cademartiri, *Lab Chip*, 2018, **18**, 620–626.
28 C. E. Stanley, J. Shrivastava, R. Brugman, E. Heinzelmann, V. Frajs, A. Bühler, D. van Swaay and G. Grossmann, *Bio-Protoc.*, 2018, **8**, e3010.
29 H. H. Chai, F. Chen, S. J. Zhang, Y. D. Li, Z. S. Lu, Y. J. Kang and L. Yu, *Lab Chip*, 2019, **19**, 2383–2393.
30 M. Moussus and M. Meier, *Lab Chip*, 2021, **21**, 2557–2564.
31 J. Aufrecht, M. Khalid, C. L. Walton, K. Tate, J. F. Cahill and S. T. Retterer, *Lab Chip*, 2022, **22**, 954–963.
32 C. Allan, A. Tayagui, V. Nock and C. N. Meisrimler, *IEEE 35th International Conference on Micro Electro Mechanical Systems Conference (MEMS)*, 2022, pp. 896–899.
33 C. Allan, B. Elliot, V. Nock and C. N. Meisrimler, *Bio-Protoc.*, 2023, **13**, e4764.
34 T. R. Vincent, M. Avramova, J. Canham, P. Higgins, N. Bilkey, S. T. Mugford, M. Pitino, M. Toyota, S. Gilroy, A. J. Miller, S. A. Hogenhout and D. Sanders, *Plant Cell*, 2017, **29**, 1460–1479.
35 T. Nietzel, M. Elsässer, C. Ruberti, J. Steinbeck, J. M. Ugalde, P. Fuchs, S. Wagner, L. Ostermann, A. Moseler, P. Lemke, M. D. Fricker, S. J. Müller-Schüssele, B. M. Moerschbacher, A. Costa, A. J. Meyer and M. Schwarzländer, *New Phytol.*, 2019, **221**, 1649–1664.
36 E. Huitema, M. Smoker and S. Kamoun, in *A Straightfor-ward Protocol for Electro-transformation of Phytophthora cap-sici Zoospores*, ed. J. M. McDowell, Humana Press, Totowa, NJ, 2011, pp. 129–135.
37 J. Schindelin, I. Arganda-Carreras, E. Frise, V. Kaynig, M. Lon-gair, T. Pietzsch, S. Preibisch, C. Rueden, S. Saalfeld, B. Schmid, J.-Y. Tinevez, D. J. White, V. Hartenstein, K. Eli-ceiri, P. Tomancak and A. Cardona, *Nat. Meth.*, 2012, **9**, 676–682.
38 H. Bishop, A. Tayagui, Y. Sun, A. Garrill and V. Nock, *38th International Conference on Image and Vision Comput-ing New Zealand (IVCNZ)*, 2023, pp. 1–6.
39 D. Ershov, M.-S. Phan, J. W. Pylvänäinen, S. U. Rigaud, L. Le Blanc, A. Charles-Orszag, J. R. W. Conway, R. F. Laine, N. H. Roy, D. Bonazzi, G. Duménil, G. Jacquemet and J.-Y. Tinevez, *Nat. Methods*, 2022, **19**, 829–832.
40 J.-Y. Tinevez, N. Perry, J. Schindelin, G. M. Hoopes, G. D. Reynolds, E. Laplantine, S. Y. Bednarek, S. L. Shorte and K. W. Eliceiri, *Methods*, 2017, **115**, 80–90.
41 V. Kapoor, W. G. Hirst, C. Hentschel, S. Preibisch and S. Reber, *Sci. Rep.*, 2019, **9**, 3794.
42 V. Ortseifen, M. Viefhues, L. Wobbe and A. Grünberger, *Front. Bioeng. Biotechnol.*, 2020, **8**, 589074.
43 B. Mosavati, A. Oleinikov and E. Du, *Sci. Rep.*, 2022, **12**, 15278.
44 V. Nock and R. Blaikie, *IEEE Sens. J.*, 2010, **10**, 1813–1819.
45 K. Ward and Z. H. Fan, *J. Micromech. Microeng.*, 2015, **25**, 094001.
46 J. Guerreiro and P. Marhavý, *Front. Plant Physiol.*, 2023, **1**, 1285373.
47 P. Köster, T. A. DeFalco and C. Zipfel, *EMBO J.*, 2022, **41**, e110741.
48 J. Kacprzyk, R. Burke, L. Armengot, M. Coppola, S. B. Tattrie, H. Vahldick, D. C. Bassham, M. Bosch, N. J. B. Brereton, J.-L. Cacas, N. S. Coll, P. Gallois, K. Kuchitsu, M. K. Nowack, H. J. Rogers, F. Van Breusegem, A. H. L. A. N. Gunawardena and P. F. McCabe, *New Phytol.*, 2024, **242**, 1865–1875.
49 Y. Liu, Y.-M. Zhang, Y. Tang, J.-Q. Chen and Z.-Q. Shao, *Curr. Opin. Plant Biol.*, 2023, **73**, 102363.
50 J. Ke, B. Wang and Y. Yoshikuni, *Trends Biotechnol.*, 2021, **39**, 244–261.
51 Y. Sun, A. Tayagui, S. Sale, D. Sarkar, V. Nock and A. Garrill, *Micromachines*, 2021, **12**, 639.
52 A. Tayagui, Y. Sun, D. A. Collings, A. Garrill and V. Nock, *Lab Chip*, 2017, **17**, 3643–3653.
53 C. Cohen, F. X. Gauci, X. Noblin, E. Galiana, A. Attard and P. Thomen, *bioRxiv*, 2023, preprint, DOI: **10.1101/2023.06.21.545863**.
54 J. Zhu, A. Moreno-Pérez and G. Coaker, *Commun. Biol.*, 2023, **6**, 814.
55 Y. Sun, A. Tayagui, A. Garrill and V. Nock, *J. Microelectromech. Syst.*, 2018, **27**, 827–835.
56 Y. Sun, A. Tayagui, A. Garrill and V. Nock, *Lab Chip*, 2020, **20**, 4141–4151.
57 A. Ghanbari, V. Nock, S. Johari, R. J. Blaikie, X. Chen and W. Wang, *J. Micromech. Microeng.*, 2012, **22**, 095009.
58 S. Johari, V. Nock, M. M. Alkaisi and W. Wang, *Lab Chip*, 2013, **13**, 1699–1707.

59 M. Kouhen, A. Dimitrova, G. S. Scippa and D. Trupiano, *Biology*, 2023, **12**, 217.
60 N. Tuteja and S. Mahajan, *Plant Signaling Behav.*, 2007, **2**, 79–85.
61 M. R. Knight, A. K. Campbell, S. M. Smith and A. J. Trewavas, *Nature*, 1991, **352**, 524–526.
62 A. Bellandi, D. Papp, A. Breakspear, J. Joyce, M. G. Johnston, J. de Keijzer, E. C. Raven, M. Ohtsu, T. R. Vincent, A. J. Miller, D. Sanders, S. A. Hogenhout, R. J. Morris and C. Faulkner, *Sci. Adv.*, 2022, **8**, eabo6693.
63 G. B. Monshausen, T. N. Bibikova, M. H. Weisenseel and S. Gilroy, *Plant Cell*, 2009, **21**, 2341–2356.
64 H. Bandurska, *Plants*, 2022, **11**, 922.
65 M. F. Seleiman, N. Al-Suhaibani, N. Ali, M. Akmal, M. Alotaibi, Y. Refay, T. Dindaroglu, H. H. Abdul-Wajid and M. L. Battaglia, *Plants*, 2021, **10**, 259.
66 C. Nakamura, S. Takenaka, M. Nitta, M. Yamamoto, T. Kawazoe, S. Ono, M. Takenaka, K. Inoue, S. Takenaka and S. Kawai, *Biotechnol. Biotechnol. Equip.*, 2021, **35**, 238–246.
67 Y. Fang, Y. Du, J. Wang, A. Wu, S. Qiao, B. Xu, S. Zhang, K. H. M. Siddique and Y. Chen, *Front. Plant Sci.*, 2017, **8**, 672.
68 N. Yazdanbakhsh and J. Fisahn, *Ann. Bot.*, 2010, **105**, 783–791.
69 Y. M. Lozano, C. A. Aguilar-Trigueros, I. C. Flaig and M. C. Rillig, *Funct. Ecol.*, 2020, **34**, 2224–2235.